Effects of a Binary Argon-Helium Shielding Gas Mixture on Ultra-Thin Features Produced by Laser-Powder Bed Fusion Additive Manufacturing

Thesis

By

Jacque Berkson

Undergraduate Program in Welding Engineering

The Ohio State University

2021

Thesis Committee

Dr. Antonio Ramirez, Advisor

Dr. Boyd Panton, Committee Member

Abstract

The practice of Additive Manufacturing (AM) is currently the subject of extreme research interest as it becomes increasingly available and feasible across multiple industries. Key characteristics of AM processes include accelerated prototyping and increased design possibilities, with metal-based processes such as Laser Powder Bed Fusion (L-PBF) proposing functional part production. However, the current state of technology lacks the validation necessary to fully implement AM in place of traditional manufacturing for established materials in industry. Through the implementation of fundamental Materials Science and Welding Engineering concepts, an intersection between manufacturing process and material properties informs the gap in information needed for further validation. The study of ultra-thin features is accomplished through the manipulation of a Concept Laser Mlab Cusing LPBF machine within the Welding Engineering department at The Ohio State University, to produce a series of fins each produced by the single pass of the process laser composed of 316L stainless steel. Such fins allow metallographic analysis to study and report the microstructural evolution of an AM part at the finest resolution the process is capable of. Similarly, by only allowing single passes of a laser, remelting, and reheating of material during printing is effectively studied without experiencing interference of subsequent exposure to the process laser. Having successfully isolated this aspect of the printing process, effects of adjusting shielding gas composition are studied by alternating argon and argon-helium gas mixtures during the building process. Explained by differences in thermal conductivity of the gasses, the effective thickness of each fin is shown to be larger when printing under the pure argon condition, supported by metallographic evidence. However, fins printed under an equal mix of argon and helium produce more consistent fins, with those designed to be overhanging proven to be produced at an angle more near that of design than those produced under the pure argon condition. Under the current state of research, fin deformation by thermal stresses is being studied, as such deformation is detrimental to the accuracy of practical part manufacturing. Furthermore, the capabilities of the LPBF

machine are being expanded to handle higher concentrations of helium to develop a wider range of data to study. As the effect of shielding gas is better understood, its manipulation and effects on the resultant part will be validated, further allowing the manipulation of this key parameter of the LPBF process in industry.

Acknowledgements

I would like to sincerely thank Dr. Antonio Ramirez for providing the opportunity to participate and learn through undergraduate research associated with the Additive Manufacturing Laboratory at Edison Joining Technology Center. Furthermore, I would like to thank Heimdall Mendoza and Dr. Edward Herderick for allowing me to contribute to preliminary work as Mr. Mendoza pursued their Master of Science with this work, as well as for their guidance as I undertake its continuation.

Table of Contents

List of Figures

List of Tables

Chapter 1. Introduction

1.1 Laser-Powder Bed Fusion

Laser-Powder Bed Fusion (LPBF) is an Additive Manufacturing (AM) process that utilizes a laser that selectively melts a feedstock of metal powder with the goal of producing a near net shape. Prior to implementing the LPBF process, a computer assisted design (CAD) depicting the desired product is manipulated within a slicing software in order to determine the part placement and orientation, and then separate the part into slices parallel to the x-y plane that the LPBF machine will successively melt upon each other in an increasing z direction as shown by Figure 1 [1]. For each successive layer, the building area is lowered by the layer thickness and the entire region is recoated in powder from the feedstock. While this layer thickness does impact the effective resolution of the part and determine the volume of powder the laser must melt for each layer, the majority of process parameters exist in the approach of how the laser melts the powder. As a function of the material properties of the powder feedstock, the laser power and scanning speed determine the energy input per unit time needed to melt the material for each layer. Adjustments in the scanning strategy include the distance between passes of the laser, known as hatch spacing, with scanning direction and the sequence in which various features of a part are scanned also have a significant impact on both the surface finish and residual stresses present in the final part. Another significant component of the LPBF process is the environment in which the feedstock is melted. Common LPBF practices utilize inert gasses such as argon to reduce the oxygen content to below 0.2%, not only to control reactions between the atmosphere and molten weld pool, but also to prevent combustion within the process chamber. In addition to the chemical interaction between the weld pool and atmosphere, the properties of the shielding gas also have influence on the solidification and cooling of the material. As heat generated through

the laser-material interaction only has the ability to flow into the existing part, build plate, and surrounding excess powder through conduction, as well as the atmosphere through convection. Therefore, the thermal interaction between the shielding gas and the selectively melted material will ultimately influence the cooling rate of the part, leading to changes in microstructure and overall adherence to the desired net shape.

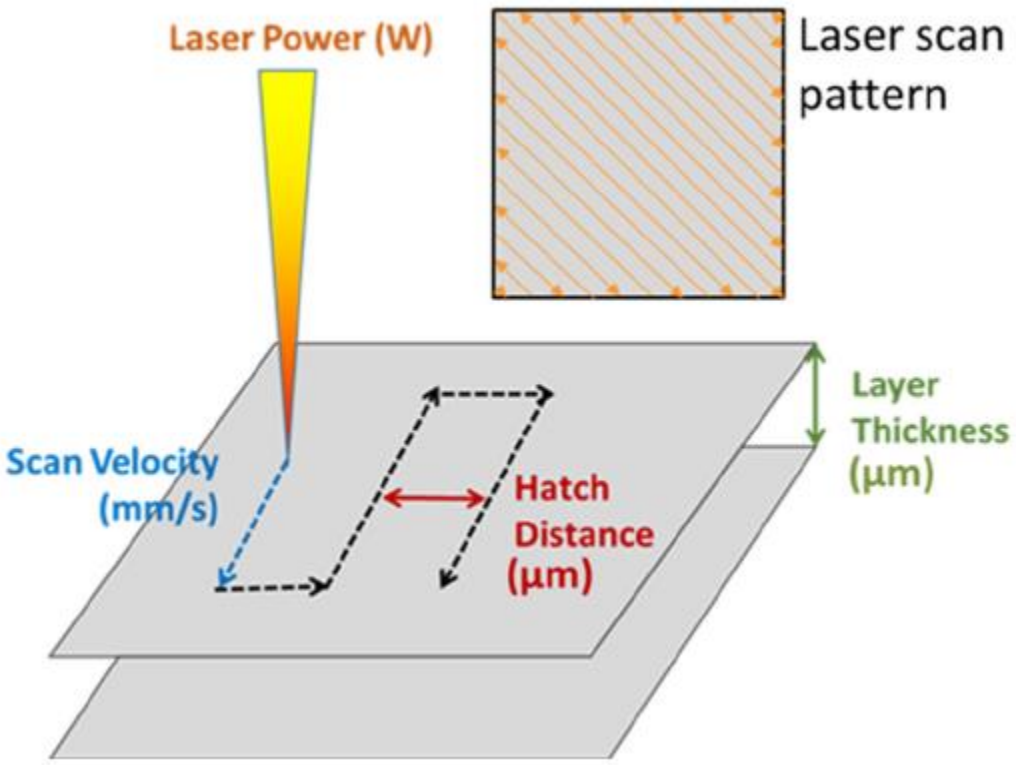

Figure 1: The laser-powder bed fusion process. Adapted from [1]

1.2 Shielding Gas Mixtures

Determined as a key parameter within the LPBF process, existing research regarding the influence of shielding gas on laser welding processes further informs and influences investigation into similar effects in this AM process. Comparisons between argon and helium

used as shielding gasses for laser welding made by Narsimhacary *et al.* and Pastor *et al.* yield an understanding that helium serves as a more effective thermal conductor, removing heat from the plasma plume generated by the laser-material interaction within the process [2], [3]. It is significant to note that this comparison is applied to the laser welding process utilizing a C02 laser, limiting the extent to which it explains differences in this L-PBF process. However, Gambhir, Sexena, Tournier, and El-Genk suggest that argon-helium gas mixtures allow for higher thermal conductivities than the pure form of either gas [4], [5]. Furthermore work by Faura *et al.* and Giacobbe find that highest thermal conductivities should be found for mixtures ranging between 50-70% helium [6], [7]. Translating these concepts from laser welding to the LPBF process, Caballero *et al.* compares commercially pure argon and helium while producing single-laser tracks, isolating a single pass of the laser for a single layer [8]. As shown by Figure 2, those single tracks produced under an argon atmosphere were inconsistent, with both conduction and keyhole profiles observed, with pure helium yielding more consistent results promoting only the preferential conduction mode [8]. Another consideration when comparing these gasses is the generation and effect of fumes within the plume, as they alongside spatter may eclipse the laser and decrease transmitted energy into the material. Traore *et al.* states that while similar cross sectional areas suggest similar energy absorption under both helium and argon atmospheres, there is lessened intensity of the plume and spatter are each reduced under the helium condition [9]. Additionally, increased plume velocities under the helium condition also encourage a denudation effect, where surrounding powder moves laterally into the weld pool. This denudation effect, shown in Figure 3, is desirable as the weld pools maintain stability in the conduction mode [9].

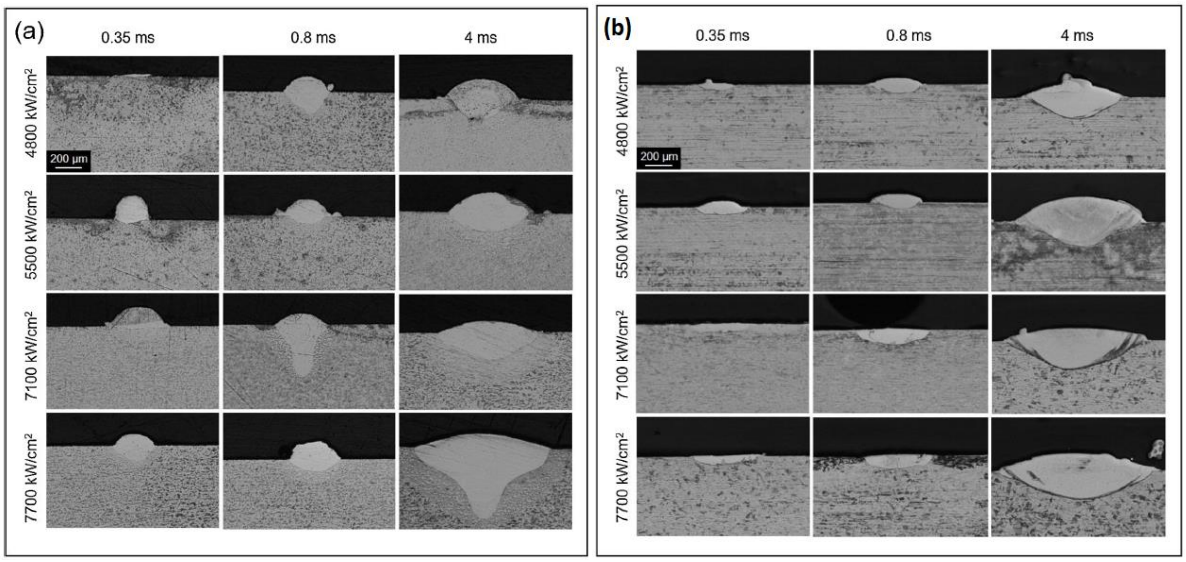

Figure 2: Weld pool cross-sections for various laser heat inputs in (a) pure argon shielding and (b) pure helium shielding. Adapted from [8]

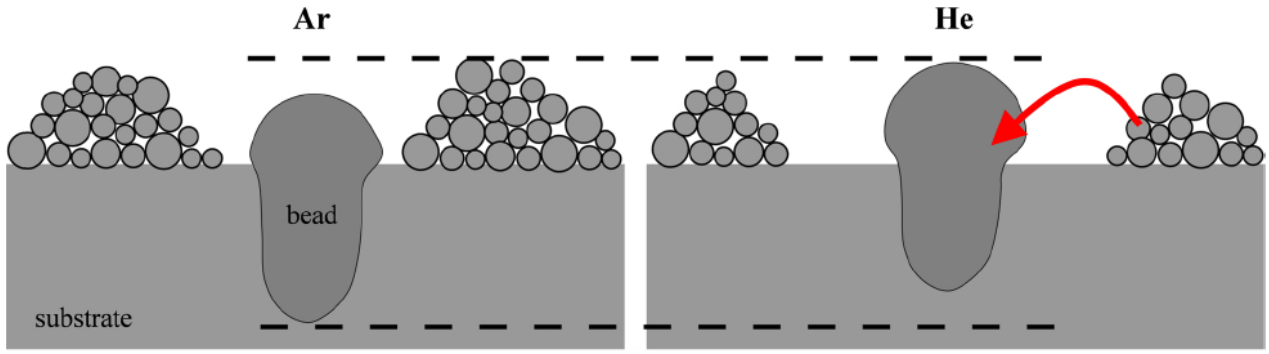

- More denudation under helium gas
- Part of the powder from the denuded areas is incorporated into the bead
- Same global molten surface
- Higher volume above the substrate under helium gas

Figure 3: Denudation effect under argon and helium shielding. Adapted from [9].

1.3 Ultra-Thin Features

There is a dual motivation to study ultra-thin features, as do they not only isolate the effects of the single pass of the process laser, but also industry interests where the fine feature resolution characteristic of the LPBF process are desirable. The work of Caballero *et al.* and Traore *et al.* each illustrate the value of isolating singular laser tracks to study the morphology and microstructural evolution across successive layers in a LPBF build. Industry interests lie not in the study of these ultra-thin features, but through their application as heat sinks. As the single laser tracks are stacked upon each other in successive layers, fins are formed with a geometry that maximizes surface area in relation to the volume of the deposited part. In application, heat flows from a substrate into the heat sink through conduction, with the maximization in surface area allowing for the highest level of convective cooling through contact with a fluid. LPBF has already been implemented utilizing a range of materials, with Collins *et al.* achieving a 400 micron thick fin out of AlSi10Mg, Escher *et al.* achieving a fin of the same material at 140 microns, and Wu *et al.* producing 100 micron thick fins out of Ti-6Al-4V, AlSi10Mg, and Inconel 718 [10], [11], [12]. However, these accomplishments have not yet taken advantage of the benefits of adjusting shielding gas as a parameter [8], [9].

1.4 Existing Work and Continuation

To further optimize the implementation of an argon-helium gas mixture to produce ultra-thin parts, Mendoza expands existing research on single layer effects by adjusting the gas mixture while producing ultra-thin fins such as those utilized as heat sinks [13]. Mendoza concludes that a 50% argon-helium mixture produces more consistent fins with improved surface roughness. However, it is explained that the thick-walled cylinder surrounding their fins, as shown by Figures 4 and 5, lead to buckling in the fins and prevent further investigation into

overhanging features. This work seeks to continue that of Mendoza, first by solving the buckling issue, then by continuing the work into the study of fins produced at non perpendicular angles in reference to the x-y build plane. Further data analysis is conducted by applying the Kurtz-Fisher model to extrapolate the cooling rate from the dendrite arm spacing reported by Mendoza [13].

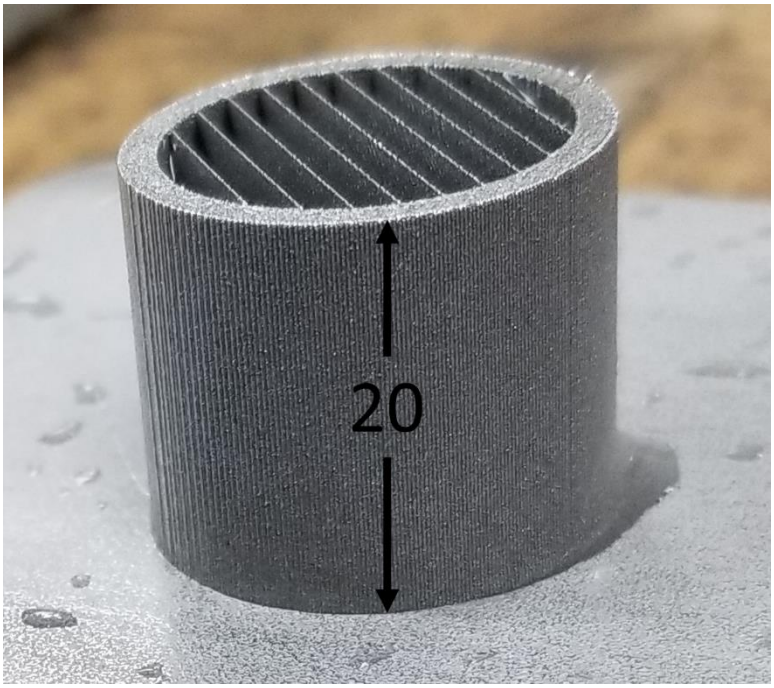

Figure 4: Original specimen produced by Mendoza. Adapted from [13]

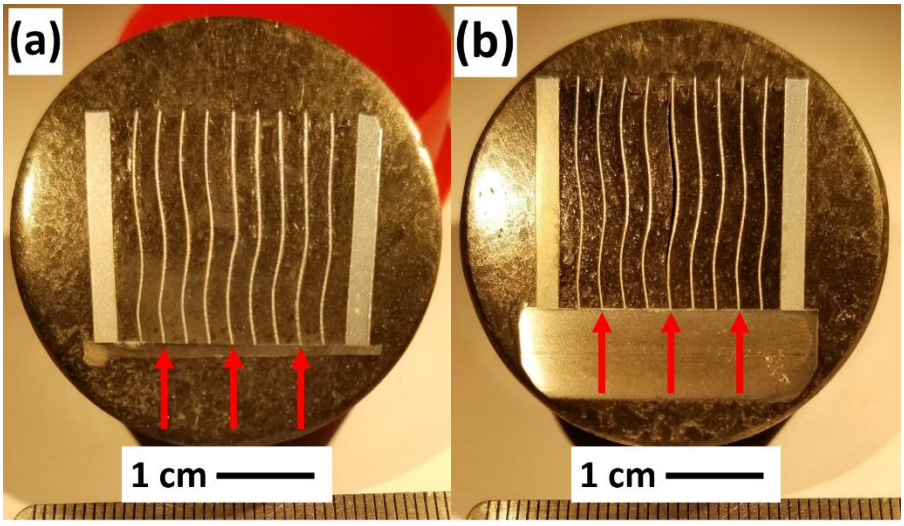

Figure 5: Buckling observed within metallographic cross-sections of (a) pure argon and (b) argon-helium shielding specimens used for imaging and analysis [13]

Chapter 2. Methodology

2.1 Materials and Processing

The Concept Laser Mlab Cusing 100R (Lichtenfels, Germany) housed within The Ohio State University Welding Engineering program's Additive Manufacturing Laboratory was utilized to fabricate all experimental specimens. This machine operates under the principles of the LPBF process, as illustrated by Figure 1 [1]. The material loaded into the machine is that of 316L Stainless Steel as sold by Concept Laser under the designation CL-20ES. All powder used is recycled powder, having been sieved across a 50-micron mesh using a Retsch AS-200 vibratory Sieve (Haan, Germany). K-type bottles of shielding gas are regulated at 2 bar and connected through hosing to the Concept Laser machine per specifications. Argon gas used was obtained from Praxair Inc. (Danbury, CT) at a purity of 4.8, with Delille Oxygen (Columbus, OH) providing 50% high purity helium balanced with argon, with the mixture being by volume and certified through gravimetric analysis.

2.2 Specimen Design

All specimens are designed using Autodesk Fusion 360 (Mill Valley, CA) as well as Materialise Magics (Leuven, Belgium). In order to prevent buckling and facilitate metallographic preparation, the sample design was altered from a cylinder to a box with an opening at the top, containing a set of fins, designed to be 100 microns thick each. The fins are oriented in reference from the x-y build plane to range from 45 degrees to 90 degrees in 5 degree increments, with the base of each fin being spaced 2mm apart. The drawings exported to the slicing software and resulting build are shown in Figures 6-7 and 8 respectively. To further prevent buckling from high heat input, the fins and outer shell are assigned separate scanning parameters, as the hatch spacing for the fins is significantly decreased from the standard Concept Laser parameter to

ensure that each is comprised of only a single pass of the laser per layer. By decreasing the hatch spacing, the proximity of lateral laser passes is reduced, which allows for single tracks to be built to design, however increasing heat input in those regions with multiple passes of the laser. The part is separated from the build plate through removable supports, so that the build plate need not be destroyed for metallography. Also note that the laser passes extend into the plane within Figure 6 and vertically within Figure 7, as well as the supporting box that extends higher than the tip of each fin, so that epoxy may cover the entire fin when it is prepared.

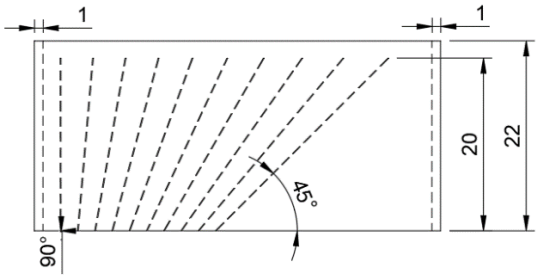

Figure 6: Side view of newly designed specimen

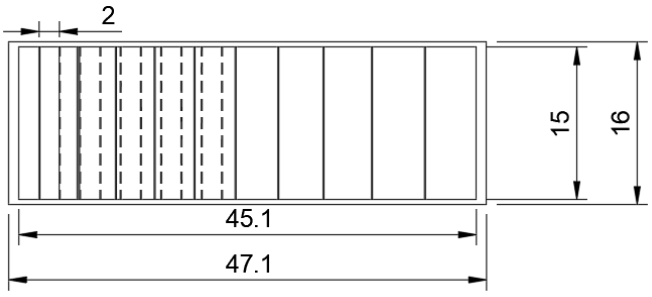

Figure 7: Top view of newly designed specimen

Figure 8: As produced build connected to build plate through removable supports

2.3 Metallographic Preparation

Prior to removal from the build plate, each sample is filled with cold mount epoxy, specified as Pace Technologies (Tucson, AZ) Epoxy-Elite to support the delicate fins for further processing. The samples are then removed from the build plate utilizing a hand saw and cross sectioned parallel to the length of the box and perpendicular to the width of the fin utilizing an Allied High Tech Products (Rancho Dominguez, CA) Techcut 5 sectioning saw. Each sample is then polished to a 0.5-micron finish by hand with a Pace Technologies Nano 1000T Grinder-Polisher. The microstructure is revealed through electro-etching in 10% oxalic acid at 3 volts for 55 seconds.

2.4 Optical Analysis

Etched samples are observed and imaged on an Olympus (Tokyo, Japan), GX51 inverted optical microscope. Collected images are stitched together and analyzed utilizing ImageJ, available in the public domain. The images are taken with an overlap of 20% and combined utilizing the grid/collection stitching tool in ImageJ moving upward and to the right. As the stitched images

result in large file sizes to the scale of multiple gigabytes of information, the TIF files are converted to grayscale and analyzed on a device with 32 gigabytes of RAM to ensure smooth processing. The location for points of measurement for thickness and angle are determined by overlaying a series of horizontal lines spaced 500 microns apart moving from the base of the fin upwards.

Chapter 3. Results and Discussion

3.1 Specimen Redesign

Observation of the epoxy filled, cross sectioned samples as seen in Figures 9 and 10, display buckling as those samples produced by Mendoza shown within Figure 5 [13]. However, the magnitude of the buckling is noticeably less, with the majority of deformation for overhanging features being confined to regions near the base. The reduction in deformation is attributed to the specimen redesign, as the reduced side wall thickness reduces compressive stresses on the fins. Furthermore, separate scanning parameters are utilized for each the fins and retaining walls, so that the reduced hatch spacing required to force single laser passes for each fin do not adversely impact the exposure of the side walls. It is also notable that the implementation of a supported structure serving as the base for the fins facilitates part removal and eliminates the effects of varying build plate surfaces.

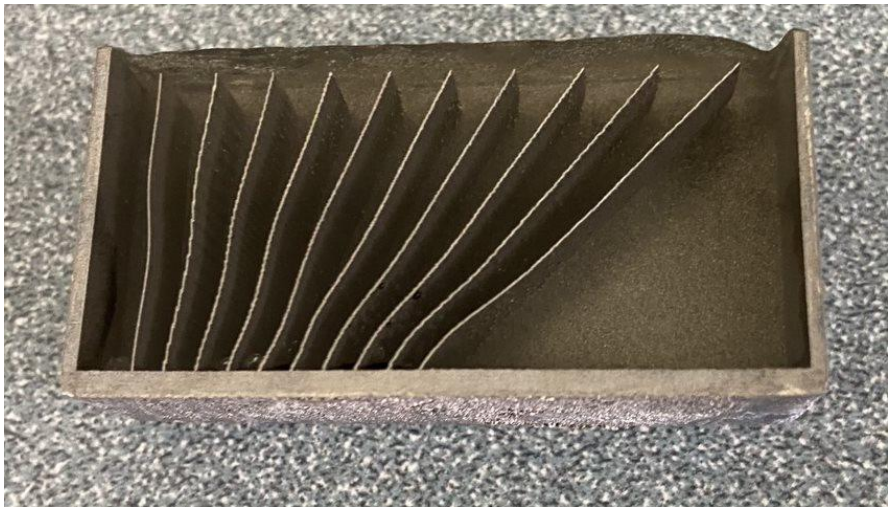

Figure 9: Cross section of redesigned sample, produced under a 100% Argon environment

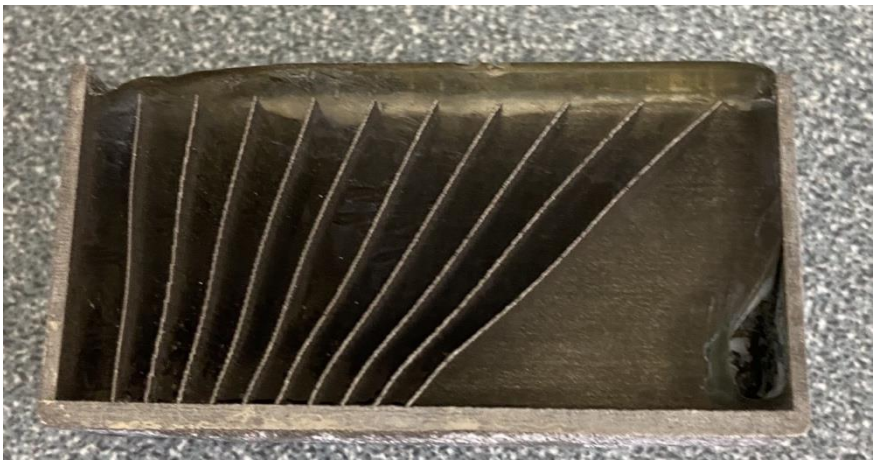

Figure 10: Cross section of redesigned sample, produced under an Argon-Helium environment

3.2 Fin Measurements

To investigate the effects of the Ar-He binary gas mixture on overhanging features, the 60-degree overhanging fin is analyzed in a method similar to that of Mendoza [13]. The 60-degree fin is chosen to represent a moderate overhanging feature, however less severe than that of a 45-degree angle. It is notable that in slicing the file designing these fins, the constrains of the scanning strategy do not yield a series of laser passes perfectly oriented following a 60-degree path. Instead, the layer height and hatch spacing determine the x and z placements of each laser pass respectively, where the slope of the fin is a function of these two parameters. The result of this is a stepping pattern in the fin, where the thickness of the fin is noticeably increased in regions where x position of the fin changes. This stepping is reflected in the fin x-projection measurements as displayed by Figure 11 and Table 1. Figure 11 displays a downward trend in thickness for the Ar-He sample with increasing build height, with the Ar sample trending at a higher overall thickness, with the averages given by Table 1 supporting this claim. The range in thicknesses in Table 1 represent not only the effects of the stepping pattern, but also the consistency in the build, with the Ar-He sample displaying a significantly larger range. However,

the increased variation in thickness is determined to be dominated by the stepping effect, as the difference in average fin thickness is similar to the difference in range for each condition. Further observation of Figure 12 and Table 1 yield average overhang values of 64 degrees for the Ar-sample and 59 degrees for the Ar-He sample. Noting the orientation of these measurements, the Ar fin is 4 degrees closer to vertical than designed, with the Ar-He overhang being 1 degree more severe than by design. However, there is a wider range in measurements for the Ar-He sample, which may be due to the low resolution of points taken, where reference points overlapping with regions displaying the stepping effect increasing the range in angle measurements.

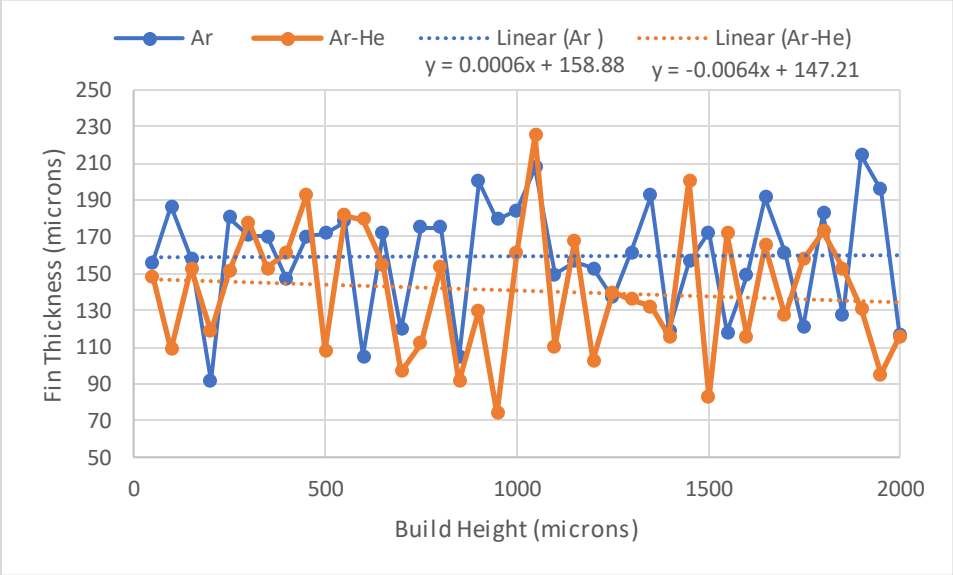

Figure 11: Fin x-projection measurements for Ar and Ar-He 60-degree overhangs

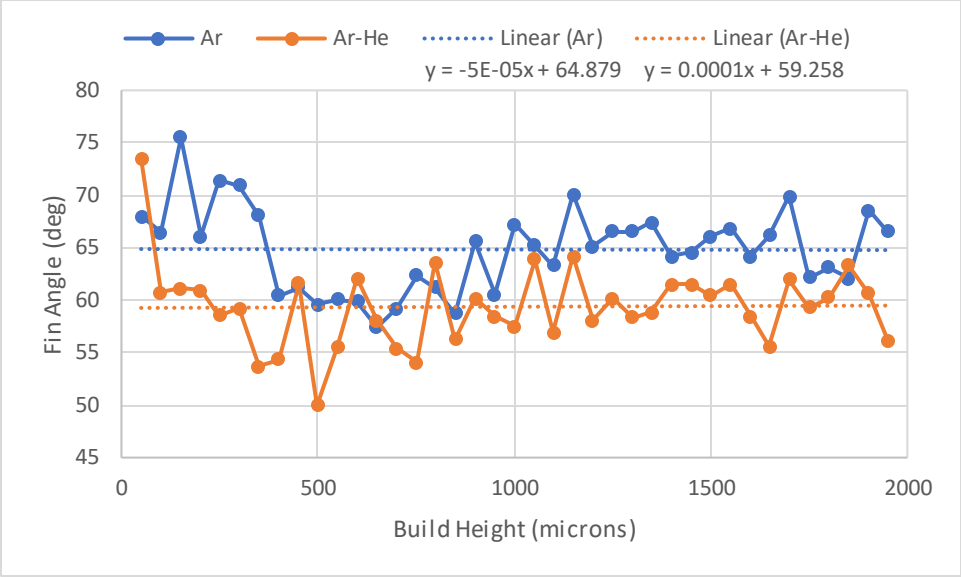

Figure 12: Fin angle measurements for Ar and Ar-He 60-degree overhangs

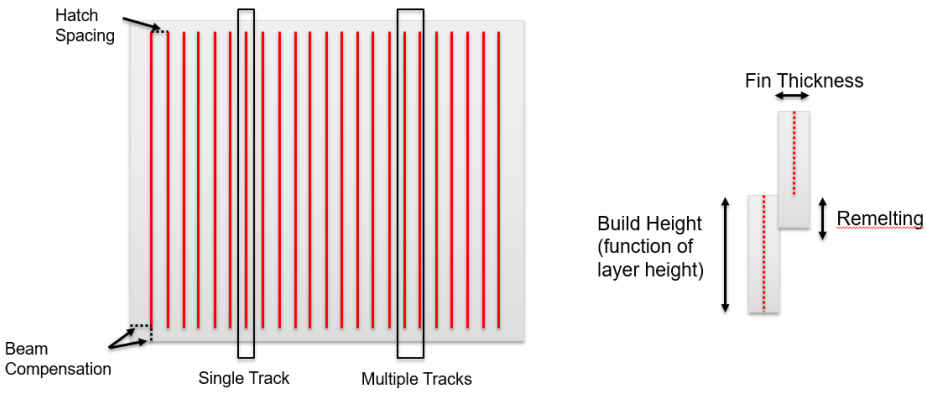

Figure 13: Scanning strategy for single tracks depicting x-y build plane (left) and x-z cross section for fin measurement (right)

Table 1: Summarized results for 60-degree overhang fins

	Ar Fin x-Projection (μm)	Ar Fin Angle (deg)	Ar-He x-Projection (μm)	Ar-He Fin Angle (deg)
Min	**91.4**	**57.4**	**73.7**	**50.0**
Max	**214.5**	**75.5**	**225.0**	**73.5**
Range	**123.1**	**18.1**	**151.3**	**23.5**
Average	**159.5**	**64.8**	**140.6**	**59.4**

Chapter 4. Conclusions

4.1 Conclusion

Through a redesign of the preliminary sample containing ultra-thin features, there is an observed reduction in fin buckling as well as improved efficiency in sample preparation. To evaluate overhanging features, a fin oriented at 60 degrees in relation to the building plane is analyzed in both thickness and build angle. This analysis yields an understanding of a stepping effect associated with the LPBF scanning parameters, with fins produced under a 100% Argon atmosphere being thicker than those produced under an atmosphere composed of 50% Argon balanced with Helium. The thinner Ar-He fins promote increased variation in fin thickness and angle measurements when combined with the stepping effect. Furthermore, the Ar-He fins are built at a more severe overhang than by design, with the fins build under the exclusively Argon atmosphere displaying a less severe overhang than by design. By placing these trends in reference of those conclusions made by Mendoza, increased cooling rate under the Ar-He atmosphere may prevent remelting of previous layers, yielding an overall thinner fin with a more pronounced stepping effect, which is desirable to produce ultra-thin features through the L-PBF process.

4.2 Future Work

The following recommendations are made for the continuation of this work:

- Further investigation into the deformation of the fins is recommended, as differences in overhang angle under different shielding conditions suggest deformation beyond that of buckling may exist.

- Continuation of the experimental methodology to evaluate fins with overhang angles ranging from 45-90 degrees, alongside the production of subsequent samples of the same design to validate results.
- This work is limited to the 50-50 argon-helium mixture as higher balances of helium are not recognized by the oxygen sensor within the Concept Laser Mlab Cusing. Preliminary investigation with the manufacturer suggests that the sensor may need to be recalibrated to operate in a wider temperature range, as helium rich mixtures interfere with the heating element enclosed in the oxygen sensor.
- As Mendoza obtained high-magnification SEM images measuring PDAS, further literature review is needed to determine the cooling rate through the Kurz-Fisher model [13],[14]. Material-specific constants are needed to implement this model. Furthermore, it is recommended to obtain measurements at varying heights in each fin, so that reheating effects may be better understood.
- Further investigation of laser occlusion by fume generation may be accomplished through the implementation of high speed imagery, with a marked contrasting background within the build chamber to analyze the movement of fumes during the build process.

4.3 Contributions

This work is presented with the acknowledgement that initial work was conducted by Mr. Heimdall Mendoza in pursuit of their Master of Science over the autumn semester of the year 2020, with Jacque Berkson assisting in the execution of work under the guidance of Mr. Mendoza. Entering the spring semester of the year 2021, Mr. Berkson further continued work as

presented within this document, influenced by suggested future work proposed by Mr. Mendoza [13].

Bibliography

[1] J. P. Oliveira, A. D. LaLonde, and J. Ma, "Processing parameters in laser powder bed fusion metal additive manufacturing," *Mater. Des.*, vol. 193, pp. 1–12, Aug. 2020, doi: 10.1016/j.matdes.2020.108762.

[2] D. Narsimhachary, R. N. Bathe, G. Padmanabham, and A. Basu, "Influence of temperature profile during laser welding of aluminum alloy 6061 T6 on microstructure and mechanical properties," *Mater. Manuf. Process.*, vol. 29, no. 8, pp. 948–953, Jul. 2014, doi: 10.1080/10426914.2013.872258.

[3] M. Pastor, H. Zhao, R. P. Martukanitz, and T. Debroy, "Porosity, underfill and magnesium loss during continuous wave Nd:YAG laser welding of thin plates of aluminum alloys 5182 and 5754," *Weld. J.*, vol. 78, no. 6, pp. 207–216, Jun. 1999.

[4] R. S. Gambhir and S. C. Saxena, "Thermal conductivity of binary and ternary mixtures of krypton, argon and helium," *Mol. Phys.*, vol. 11, no. 3, pp. 233–241, 1966, doi: 10.1080/00268976600101071.

[5] J. M. P. Tournier and M. S. El-Genk, "Properties of noble gases and binary mixtures for closed brayton cycle applications," *Energy Convers. Manag.*, vol. 49, no. 3, pp. 469–492, Mar. 2008, doi: 10.1016/j.enconman.2007.06.050.

[6] F. Faura, A. Campo, and B. Zamora, "A mixture of pure gases that produce maximum heat transfer characteristics for quenching," *J. Mater. Eng. Perform.*, vol. 7, no. 3, pp. 420–424, Jun. 1998, doi: 10.1361/105994998770347873.

[7] F. W. Giacobbe, "Heat transfer behavior of gaseous mixtures containing helium and argon or nitrogen," *J. Thermophys. Heat Transf.*, vol. 17, no. 1, pp. 112–119, Jan. 2003, doi: 10.2514/2.6741.

[8] A. Caballero, W. Suder, X. Chen, G. Pardal, and S. Williams, "Effect of shielding conditions on bead profile and melting behaviour in laser powder bed fusion additive manufacturing," *Addit. Manuf.*, vol. 34, Aug. 2020, doi: 10.1016/j.addma.2020.101342.

[9] S. Traore, M. Schneider, I. Koutiri, F. Coste, R. Fabbro, C. Charpentier, P. Lefebvre, and P. Peyre, "Influence of gas atmosphere (Ar or He) on the laser powder bed fusion of a Ni-based alloy," *J. Mater. Process. Technol.*, vol. 288, Feb. 2021, doi: 10.1016/j.jmatprotec.2020.116851.

[10] I. L. Collins, J. A. Weibel, L. Pan, and S. V. Garimella, "A permeable-membrane microchannel heat sink made by additive manufacturing," *Int. J. Heat Mass Transf.*, vol. 131, pp. 1174–1183, Mar. 2019, doi: 10.1016/j.ijheatmasstransfer.2018.11.126.

[11] F. Calignano, G. Cattano, and D. Manfredi, "Manufacturing of thin wall structures in AlSi10Mg alloy by laser powder bed fusion through process parameters," *J. Mater.*

Process. Technol., vol. 255, pp. 773–783, May 2018, doi: 10.1016/j.jmatprotec.2018.01.029.

[12] Z. Wu, S. P. Narra, and A. Rollett, "Exploring the fabrication limits of thin-wall structures in a laser powder bed fusion process," *Int. J. Adv. Manuf. Technol.*, vol. 110, no. 1–2, pp. 191–207,Aug. 2020, doi: 10.1007/s00170-020-05827-4.

[13] H. Mendoza, "Effects of a Binary Argon-Helium Shielding Gas Mixture on Ultra-Thin Features Produced by Laser-Powder Bed Fusion Additive Manufacturing", 2020

[14] W. Kurz and D. J. Fisher, "Dendrite growth at the limit of stability: tip radius and spacing" *Acta Metall.*, vol. 29, no. 1, pp. 11–20, Jan. 1981.

Appendix A. Stitched Fin Images

As each stitched fin image compromises approx. 3GB of data, they are not included in this document. Please contact Jacque Berkson at Berkson.7@osu.edu or jberkson1@gmail.com for access to these files.

Appendix B. Measurement Data for Fin Measurements

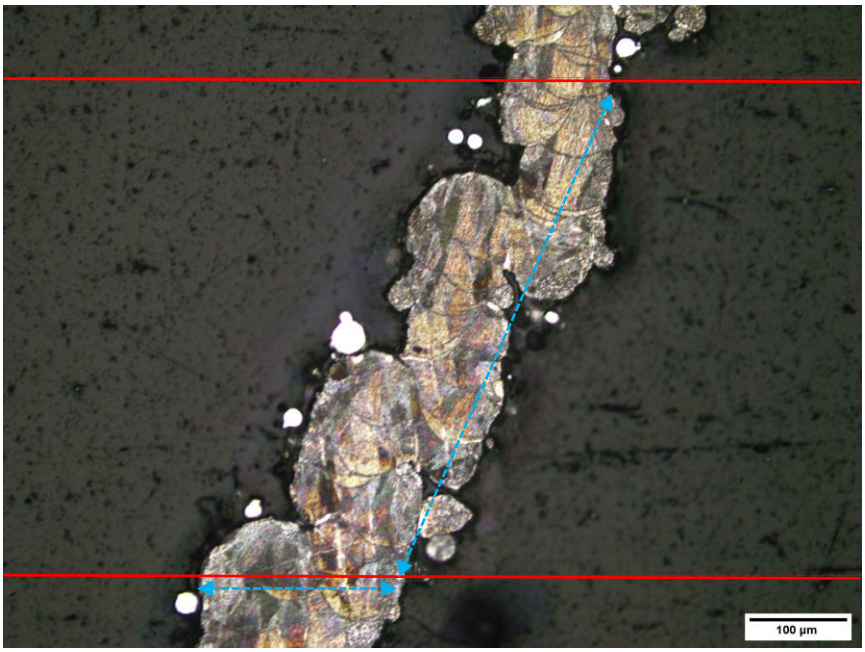

Figure 14: Measurement methodology displaying angle and x-projection directions

Table 2: Thickness data for 60 degree argon fin

#	Area	Mean	Min	Max	Angle	Length
1	63.021	185.499	39	255	0	148.305
2	46.143	169.066	43	237	0	108.475
3	64.996	145.989	53	253	0	152.966
4	50.273	132.432	43	235	0	118.22
5	64.278	184.237	35	255	0	151.271
6	75.589	148.183	36	255	0	177.966
7	64.816	181.219	8	255	0	152.542
8	68.587	126.584	47	253	0	161.441
9	82.053	135.873	41	240	0	193.22
10	45.964	88.566	14	185	0	108.051
11	77.205	98.202	29	226	0	181.78
12	76.128	95.611	35	247	0	179.237
13	65.893	84.117	23	173	0	155.085
14	41.116	74.48	40	128	0	96.61
15	47.58	82.521	17	146	0	111.864
16	65.355	95.959	35	219	0	153.814
17	38.962	100.051	32	208	0	91.525
18	55.121	113.163	59	183	0	129.661
19	31.421	64.583	25	124	0	73.729
20	68.587	83.976	13	183	0	161.441
21	95.519	90.889	33	204	0	225
22	47.041	87.126	22	153	0	110.593
23	71.28	101.471	13	252	0	167.797
24	43.809	79.951	25	186	0	102.966
25	59.43	96.136	39	222	0	139.831
26	57.814	98.832	14	233	0	136.017
27	56.198	95.617	44	206	0	132.203
28	49.196	89.259	41	162	0	115.678
29	85.284	90.084	8	165	0	200.847
30	35.191	102.321	20	209	0	82.627
31	72.896	90.586	21	202	0	171.61
32	49.196	76.186	22	172	0	115.678
33	70.203	77.563	7	160	0	165.254
34	54.043	91.977	32	193	0	127.119
35	66.971	92.164	27	246	0	157.627
36	73.434	91.384	23	210	0	172.881
37	64.816	102.651	21	196	0	152.542
38	55.659	108.294	27	216	0	130.932
39	40.577	116.354	54	195	0	95.339
40	49.196	52.522	14	132	0	115.678

Table 3: Angle data for 60 degree argon fin

#	Area	Mean	Min	Max	Angle	Length
1	230.66	88.501	22.462	255	67.946	539.474
2	233.216	127.665	23.347	255	66.448	545.437
3	223.172	170.257	31.681	255	75.486	521.781
4	235.225	117.48	13.261	255	66.065	549.849
5	223.355	93.227	14.514	255	71.387	522.184
6	228.468	114.643	20	255	70.956	534.374
7	231.755	107.95	20.444	255	68.048	541.851
8	244.539	135.595	19	255	60.446	571.835
9	247.827	143.284	16.502	255	61.167	579.538
10	249.105	51.961	10.951	255	59.598	582.683
11	244.174	114.574	15.197	255	60.096	570.88
12	247.096	139.86	18.15	255	59.908	577.885
13	252.392	138.596	27.854	255	57.414	590.368
14	252.758	125.048	16.145	255	59.207	591.013
15	238.878	99.438	9.959	255	62.376	558.539
16	245.453	116.466	11.048	255	61.173	573.893
17	247.461	102.837	18.387	255	58.775	578.704
18	236.139	59.22	9.852	255	65.578	551.95
19	245.453	101.012	15.159	255	60.573	574.067
20	231.938	80.116	11.329	255	67.193	542.409
21	237.965	123.65	16.911	255	65.206	556.416
22	236.869	96.754	11.217	255	63.316	553.858
23	225.181	111.351	17.817	255	70.065	526.416
24	239.426	136.593	21.545	255	65.078	559.821
25	234.312	53.007	10.214	255	66.555	547.789
26	234.312	133.088	16.994	255	66.555	547.789
27	233.947	146.755	27.075	255	67.401	547.14
28	236.321	143.808	16.955	255	64.148	552.753
29	224.633	84.173	9.716	255	64.592	525.392
30	235.225	67.159	10.445	255	66.065	549.849
31	233.764	94.04	12.93	255	66.801	546.773
32	236.321	136.462	18.77	255	64.148	552.753
33	238.695	65.115	10.231	254.986	66.144	557.921
34	226.642	112.844	14.616	255	69.898	529.703
35	246.731	145.738	22.325	255	62.182	576.929
36	237.417	84.165	10.728	255	63.08	555.014
37	243.261	70.809	15	246.79	62.049	568.93
38	227.555	91.608	19.947	255	68.506	531.858
39	242.713	46.349	10.229	204.179	66.563	567.316

Table 4: Thickness data for 60 degree argon-helium fin

#	Area	Mean	Min	Max	Angle	Length
1	63.021	185.499	39	255	0	148.305
2	46.143	169.066	43	237	0	108.475
3	64.996	145.989	53	253	0	152.966
4	50.273	132.432	43	235	0	118.22
5	64.278	184.237	35	255	0	151.271
6	75.589	148.183	36	255	0	177.966
7	64.816	181.219	8	255	0	152.542
8	68.587	126.584	47	253	0	161.441
9	82.053	135.873	41	240	0	193.22
10	45.964	88.566	14	185	0	108.051
11	77.205	98.202	29	226	0	181.78
12	76.128	95.611	35	247	0	179.237
13	65.893	84.117	23	173	0	155.085
14	41.116	74.48	40	128	0	96.61
15	47.58	82.521	17	146	0	111.864
16	65.355	95.959	35	219	0	153.814
17	38.962	100.051	32	208	0	91.525
18	55.121	113.163	59	183	0	129.661
19	31.421	64.583	25	124	0	73.729
20	68.587	83.976	13	183	0	161.441
21	95.519	90.889	33	204	0	225
22	47.041	87.126	22	153	0	110.593
23	71.28	101.471	13	252	0	167.797
24	43.809	79.951	25	186	0	102.966
25	59.43	96.136	39	222	0	139.831
26	57.814	98.832	14	233	0	136.017
27	56.198	95.617	44	206	0	132.203
28	49.196	89.259	41	162	0	115.678
29	85.284	90.084	8	165	0	200.847
30	35.191	102.321	20	209	0	82.627
31	72.896	90.586	21	202	0	171.61
32	49.196	76.186	22	172	0	115.678
33	70.203	77.563	7	160	0	165.254
34	54.043	91.977	32	193	0	127.119
35	66.971	92.164	27	246	0	157.627
36	73.434	91.384	23	210	0	172.881
37	64.816	102.651	21	196	0	152.542
38	55.659	108.294	27	216	0	130.932
39	40.577	116.354	54	195	0	95.339
40	49.196	52.522	14	132	0	115.678

Table 5: Angle data for 60 degree argon-helium fin

#	Area	Mean	Min	Max	Angle	Length
1	218.149	131.704	11.903	255	73.491	514.429
2	237.18	117.073	15.145	255	60.756	559.439
3	237.719	77.72	5.659	254.115	61.109	560.426
4	237.36	47.605	5.431	255	60.933	559.93
5	245.799	84.529	5.254	255	58.541	579.701
6	243.465	65.359	6.636	254.76	59.232	574.015
7	256.392	82.06	11.548	255	53.636	604.6
8	258.726	34.253	4.917	170.5	54.324	610.302
9	237.899	67.209	8.34	252.869	61.576	560.828
10	273.09	66.141	9.087	250.829	49.963	644.204
11	249.928	54.729	2.508	254.969	55.453	589.552
12	239.155	39.292	5.886	187.22	62.049	564.109
13	248.492	73.501	4.37	231.163	58.034	585.874
14	254.596	81.734	6.088	233.988	55.435	600.486
15	257.11	50.454	3.742	249.219	54.043	606.179
16	235.205	83.911	10.086	244.852	63.611	554.851
17	254.058	78.603	13.945	235.44	56.243	599.359
18	237.001	81.374	5.965	232.226	60.139	558.709
19	243.465	49.155	3.735	227.623	58.492	574.037
20	245.619	65.532	2.432	228.858	57.461	579.026
21	232.871	60.62	5.042	232.552	63.909	549.182
22	249.749	45.184	3.995	239.48	56.893	588.812
23	233.589	48.498	5.693	255	64.144	550.911
24	245.799	67.448	9.856	208.06	58.088	579.541
25	239.335	46.354	3.707	228.02	60.143	564.307
26	243.644	64.51	10.062	255	58.384	574.703
27	242.567	51.791	3.288	220.044	58.818	572.054
28	239.694	35.425	5.781	179.41	61.533	565.392
29	237.36	59.888	7.163	255	61.514	559.71
30	238.437	45.275	6.696	160.446	60.48	562.418
31	237.36	45.791	8.709	211.723	61.514	559.71
32	243.465	41.016	3.969	205.486	58.492	574.037
33	252.801	33.419	1.7	243.057	55.598	596.231
34	236.283	41.617	5.296	210.575	61.974	557.303
35	243.824	47.133	6.741	215.077	59.297	575.108
36	238.976	32.951	6.286	179.202	60.255	563.675
37	232.871	50.179	5.626	200.703	63.316	549.164
38	238.258	84.189	17.891	203.463	60.593	561.793
39	251.724	104.594	12	200.893	56.174	593.719